1 **Feedback mechanisms between precipitation and dissolution reactions across**
2 **randomly heterogeneous conductivity fields**

4 **Yaniv Edery[1*], Martin Stolar[1], Giovanni Porta[2], Alberto Guadagnini[2]**

6 [1] Faculty of Civil and Environmental Engineering, Technion, Haifa, Israel

7 [2]Department of Civil and Environmental Engineering, Politecnico di Milano, 20133, Milan, Italy;

8 * Corresponding author: Yaniv Edery (yanivedery@technion.ac.il)

9 **Highlights**

11 • Regions of prevailing precipitation and dissolution are related to preferential flow patterns
12 • Large changes in non-Fickian transport parameters are observed while velocity variance
13 display modest variations
14 • Initial heterogeneity facilitates attaining asymptotic average solute velocity value

15

16 **Abstract**

17 Our study investigates interplays between dissolution, precipitation, and transport processes
18 taking place across randomly heterogeneous conductivity domains and the ensuing spatial
19 distribution of preferential pathways. We do so by relying on a collection of computational analyses
20 of reactive transport performed in two-dimensional systems where the (natural) logarithm of
21 conductivity is characterized by various degrees of spatial heterogeneity. Our results document that
22 precipitation and dissolution jointly take place in the system, the latter mainly occurring along
23 preferential flowpaths associated with the conductivity field, the former being observed at locations
24 close to and clearly separated from these. High conductivity values associated with the preferential
25 flowpaths tend to further increase in time, giving rise to a self-sustained feedback between transport
26 and reaction processes. The clear separation between regions where dissolution or precipitation takes
27 place is imprinted onto the sample distributions of conductivity which tend to become visibly left
28 skewed with time (with the appearance of a bimodal behavior at some times). The link between
29 conductivity changes and reaction-driven processes promotes the emergence of non-Fickian effective
30 transport features. The latter can be captured through a continuous time random walk model where
31 solute travel times are approximated with a truncated power law probability distribution. The
32 parameters of such a model shift towards values associated with increasingly high non-Fickian
33 effective transport behavior as time progresses.

34 **1.Introduction**

35 Diagnosis and characterization of the feedback between geochemical precipitation/dissolution
36 reactions and solute transport processes in heterogeneous subsurface systems is key to a variety of
37 environmental and Earth science scenarios (Rege & Fogler, 1989; Berkowitz et al., 2016). A critical
38 challenge is the emergence of complex dependencies between physical and chemical processes taking
39 place across aquifer bodies (Saripalli et al., 2001). Heterogeneity of these systems promotes diverse
40 patterns of precipitation and/or dissolution that may imprint a variety of dynamic system responses,
41 including, e.g., wormholing and oscillatory behaviors of system attributes such as porosity and

42 permeability (Edery et al., 2011; Garing et al., 2015; Golfier et al., 2002). Examples of practical
43 applications in this context include geologic CO_2 storage (e.g., Pawar et al., 2015; Noiriel & Daval,
44 2017; Cabeza et al., 2020 and references therein), acid injection in production wells (e.g., Liu et al.,
45 2017 and references therein), and reactive transport of contaminants (e.g., Ceriotti et al., 2018; Dalla
46 Libera et al., 2020 and references therein).

47 Computational studies can assist the analysis of patterns of chemical transport across
48 heterogeneous subsurface systems in the presence of precipitation/dissolution phenomena. While
49 requiring an explicit description of the spatial heterogeneity of the system properties (Atchley et al.,
50 2014), routine application of numerical simulations in practical settings is hampered by (*i*) our limited
51 knowledge of the system attributes, resulting in uncertainty affecting the parameterization of the
52 underlying physical and chemical processes and their variability, and (*ii*) the computational costs
53 required to properly quantify such uncertainties and their propagation onto environmental quantities
54 of interest. In this context, we rely on an effective approach to characterize the evolution of key
55 features of solute transport in the presence of rock-fluid interactions across a porous medium whose
56 spatially heterogeneous conductivity field is interpreted according to a commonly employed
57 stochastic framework.

58 A critical element we tackle is related to the analysis of the dynamic feedback between reactive
59 transport and spatially heterogenous distributions of porous media attributes such as hydraulic
60 conductivity. Following prior studies, we start by recognizing that, even under geochemical
61 equilibrium conditions, the spatial heterogeneity of system attributes typically imprints an uneven
62 spatial distribution of regions where chemical reactions take place, local fluctuations of conductivity
63 being key to this element (Edery, Porta, et al., 2016). Further to this, our conceptualization of the
64 setting is grounded on the observation that rendering of transport features in geological formations
65 through effective formulations typically requires embedding non-Fickian features. To this end, we
66 rely on a continuous time random walk (CTRW) upscaled model where solute travel times are
67 approximated with a truncated power law (TPL) probability density function (PDF), hereafter termed
68 CTRW-TPL (Berkowitz et al., 2006). This effective modeling framework is particularly relevant
69 because the emergence of non-Fickian transport features in heterogeneous formations has been
70 observed at diverse scales of observation, including pore-, laboratory- and field-scale scenarios (e.g.,
71 Edery et al., 2011; Muljadi et al., 2018; Menke et al., 2018 and references therein).

72 In line with our objective, we rest on the framework of analysis developed in (Edery et al.,
73 2014; Edery, Porta, et al., 2016), where an effective depiction of transport processes is parametrized
74 as a function of the statistics of solute residence times in randomly heterogeneous conductivity fields.
75 A main element of this framework is that it yields a link between the CTRW-TPL formulation and
76 the occurrence of preferential pathways that can be obtained from computational studies of transport
77 in such conductivity fields (Edery et al., 2014). As a result, the methodology is conducive to an
78 effective (or upscaled) representation of local features to identify signatures of non-Fickian transport
79 and embed these in the representation of solute breakthrough curves (BTC) as a function of the
80 underlying system properties (see also, e.g., Dentz et al., 2011; Edery et al., 2014). To illustrate the
81 main features associated with the scenario of interest, we consider a Darcy-scale formulation of a
82 reactive transport setup, where precipitation and/or dissolution of minerals are driven by the injection
83 of an acid compound establishing local equilibrium with the resident fluid and a solid matrix of the
84 host porous medium which is considered to be composed of calcite mineral. While the geochemical
85 processes we consider are somehow streamlined with respect to a field-scale scenario, they embed
86 the main elements characterizing the interplay between solute transport and rock-fluid interactions in
87 Darcy-scale systems. Within this conceptual picture, our study aims at investigating (*i*) the interplay

88   between the reactive process and the ensuing spatial distribution of preferential pathways associated
89   with spatially heterogeneous conductivities and (*ii*) the link between locally occurring reaction-driven
90   phenomena and emerging non-Fickian effective transport features, as captured by the CTRW-TPL
91   framework.

92   **2.Methodology**

93   **2.1 Chemical model**

94   We simulate a reactive transport scenario where calcite ($CaCO_{3\,(s)}$, subscript (*s*) denoting solid
95   mineral) can dissolve or precipitate locally in the presence of chemical equilibrium between dissolved
96   carbonic acid (H_2CO_3) and pH. The amount of dissolved H_2CO_3 as a function of pH (see Figure S1
97   in the supplementary material) is then governed by equilibrium conditions, which is tantamount to
98   assuming a locally instantaneous reaction (i.e., infinite local Damköhler number). The formulation
99   describing the chemical reactions can then be streamlined as:

100    $CaCO_{3\,(s)} \leftrightarrow Ca^{2+} + CO_3^{2-}$ (1a)

101    $H_2CO_3 \leftrightarrow 2H^+ + CO_3^{2-}$ (1b)

102   according to which two protons H^+ in (1b) react with CO_3^{2-} to produce H_2CO_3 that in turn drives
103   dissolution of the host calcium carbonate solid matrix. In this context, and consistent with typical
104   experimental practice, we consider the injected fluid and the porous medium to be associated with a
105   source of H^+ and an abundance of Ca^{2+}, respectively. Thus, Ca^{2+} is not rate limiting and the spatial
106   distribution of H^+, as driven by transport and reaction, governs pH. The rate limiting reaction is then
107   (1b), that is controlled by the available H^+ (or pH), similar to observations associated with other
108   studies (Singurindy & Berkowitz, 2004; Edery et al., 2011). The chemical reaction system (1a) and
109   (1b) is here simplified (see, e.g., Krauskopf & Bird, 1967) through:

110    $co \leftrightarrow 2h + c$ (2)

111   where *co* denotes H_2CO_3, *h* and c representing H^+ and $CaCO_{3\,(s)}$, respectively.

112   **2.2 Flow and transport modeling**

113   Our computational setting is intended to mimic a laboratory scale scenario where a 60×24 cm^2
114   two-dimensional flow cell is filled with a porous system formed by a $CaCO_{3\,(s)}$ solid matrix. The
115   system is initially fully saturated with water and an injection of low pH water takes place across the
116   upstream side of the cell. To investigate the influence of the dissolution/precipitation reaction on
117   solute transport, we consider a uniform in the mean groundwater flow, taking place within a two-
118   dimensional domain where the (natural) logarithm of conductivity, $y = \ln(k)$, is considered as a
119   zero-mean, second-order stationary random field. The latter is further characterized by an isotropic,
120   simple exponential, covariance function, with (normalized) correlation length *l/L*, *L* being the length
121   of the domain along the main flow direction. Various degrees of heterogeneity of the system are
122   analyzed upon considering values of log-conductivity variance $\sigma_0^2 = [1, 3, 5]$, subscript 0 denoting
123   that these values refer to the initially generated conductivity distributions (i.e., prior to the occurrence
124   of reactions). The domain is discretized through 300×120 elements of uniform size $\Delta = 0.2$ cm,
125   yielding a field size of 60×24 cm^2. Each field is synthetically generated through the widely tested
126   sequential Gaussian simulator GCOSIM3D (Gómez-Hernández & Journel, 1993) and is characterized
127   by *l/L* = 0.016. This yields a value of $\Delta/l = 0.2$, which is deemed adequate to capture the local features

128   of the covariance of y and their impact on the main statistics of the velocity field and travel times
129   (Ababou et al., 1989; Riva et al., 2009).

130   For each value of σ_0^2, 20 random realizations of y are generated, each being then subject to a
131   deterministic pressure drop ($\Delta H = 100$cm) between the inlet (left) and the outlet (right) sides. The
132   local distribution of fluid velocity is computed through

133   $\nabla \cdot \boldsymbol{q}(\boldsymbol{x}) = 0; \boldsymbol{q}(\boldsymbol{x}) = -k(\boldsymbol{x}) \cdot \nabla h(\boldsymbol{x})$ (3)

134   where $\boldsymbol{q}(\boldsymbol{x})$ is the local Darcy flux, vector $\boldsymbol{x}$ corresponding to spatial location. The local fluid velocity
135   field is then obtained as $\boldsymbol{v} = \boldsymbol{q}/\theta$, a constant initial porosity $\theta = 0.4$ being here considered for the
136   porous medium.

137   Solute transport is then simulated across each conductivity field by a particle tracking approach
138   (Le Borgne et al., 2008). A number of 10^5 h particles (see (2)), which is selected to represent a full
139   pore volume at constant pH = 3.5, is divided by the domain length and multiplied by the mean velocity
140   ($\hat{\boldsymbol{v}}$, as evaluated from (4) across the whole domain). A total amount of particles evaluated as
141   $Integer(10^5/L \cdot \Delta t \cdot \hat{\boldsymbol{v}})$ is then injected into the system at regular time intervals ($\Delta t = 0.1$ min).
142   Particles injected at each Δt are flux-weighted according to the conductivity distribution at the inlet.
143   The particles representing a full pore volume correspond to 10.79 moles of H^+, the same amount
144   being injected across the simulation course to obtain a constant pH = 3.5 in the injected fluid, while
145   absence of h particles is taken to correspond to pH = 8. We then evaluate the pH value (or H^+ molar
146   mass) associated with each h particle by dividing the total number of H^+ moles required to obtain a
147   pH = 3.5 (i.e., 10.79 mol of H^+) by the pore volume (as represented by 10^5 h particles).

148   The upper and lower boundaries of the domain are reflective while the outlet boundary is
149   absorbing. Transport is simulated through

150   $\boldsymbol{d} = \boldsymbol{v}[\boldsymbol{x}(t_k)]\delta t + \boldsymbol{d}_D$ (4)

151   where $\boldsymbol{d}$ is particle displacement, $\boldsymbol{x}(t_k)$ is the vector identifying spatial coordinates of particle location
152   at time t_k, $\boldsymbol{v}$ is fluid velocity at $\boldsymbol{x}(t_k)$, $\delta t = \delta s/v$ is the temporal displacement magnitude (v is the norm
153   of $\boldsymbol{v}$), and $\boldsymbol{d}_D$ is the diffusive displacement. The latter is evaluated as $\boldsymbol{d}_D = 3N[0,1]\sqrt{2D_m\delta t}$, where
154   $N[0,1]$ represents a two-dimensional vector of random variables, whose entries are mutually
155   independent and sampled from a Gaussian distribution with zero mean and unit variance, $D_m = 10^{-5}$
156   cm^2/min representing diffusion. The value of δs is selected to be an order of magnitude less than Δ,
157   to accurately sample the velocity variability within a conductivity block.

158   Coupling between particle evolution and the geochemical setup illustrated in Section 2.1 is
159   achieved in two steps. First, we advance all particles according to the displacement mechanism
160   described above. Second, we satisfy the equilibrium condition (2) by equilibrating both co and h
161   within each cell, leading to precipitation or dissolution of a calcite mineral. The calcite volume to
162   mole ratio is taken as $M = 37 \frac{cm^3}{mol}$ (Morse & Mackenzie, 1993) and the equilibrium between h and
163   co particles (according to (2)) leads to a local precipitation (or dissolution) of the solid. We update in
164   time the spatial distribution of porosity assuming that it is characterized by a uniform change within
165   each individual domain cell. We finally update conductivity through the Kozeny-Carman (KC)
166   formulation

167   $k(ar)_{ij} = k(br)_{ij} \cdot \frac{\theta(ar)_{ij}{}^3}{(1-\theta(ar)_{ij})^2} \cdot \frac{(1-\theta(br)_{ij})^2}{\theta(br)_{ij}^3}$ (5)

168 where $k(ar)_{ij}$ and $\theta(ar)_{ij}$ are conductivity and porosity, respectively, after the reaction (ar) has
169 taken place, while $k(br)_{ij}$ and $\theta(br)_{ij}$ are their counterparts before the reaction is observed,
170 subscripts i and j being identifiers of a given cell. The process is repeated for each particle in each of
171 the cells until an equilibrium between co and h is reached. We set an upper and a lower bound of 0.1
172 and 0.9, respectively, for porosity, to avoid the occurrence of unphysical porosity values. Precipitation
173 is treated numerically in a corresponding way. We numerically calculate the updated local head and
174 fluid velocity distributions from (4) at time intervals of 10 Δt, to reduce constraints associated with
175 computational costs. The computational cost of each realization is between 1~3 days (depending on
176 the value of σ_0^2), upon relying on a 16 Xeon 2.6 Ghz processor with 64 GB RAM.

177 The updated conductivity field is extracted and stored at the above mentioned regular intervals
178 of 10 Δt. Transport of a non-reactive solute pulse is then simulated across each of these updated fields
179 to capture the temporal evolution of the key parameters driving effective transport (see Section 2.3).
180 While noting that natural porous media can exhibit complex relationships between permeability and
181 porosity (Luquot & Gouze, 2009), which may not always be interpreted through the KC model (6),
182 we employ the latter formulation because it is considered as a reference model in the literature and
183 can serve as a proxy for alternative improved parameterizations (Erol et al., 2017).

184 **2.3 Quantities of interest**

185 The workflow described in Section 2.2 enables one to extract computationally-based quantities
186 employed to characterize the analyzed reactive transport setup. As stated in Section 2.2, we simulate
187 a tracer test within the original fields as well as within those modified by precipitation/dissolution.
188 Particles are displaced through the action of advection and diffusion following a pulse (flux-weighted)
189 injection at the inlet. These non-reactive transport simulations are performed to assess base values of
190 parameters characterizing solute transport (a) prior to starting the reactive transport simulation as well
191 as (b) at specific times after reaction changed the field. The empirical PDF of particle waiting times
192 is assessed from the corresponding histogram starting by evaluating particle waiting times within a
193 given domain cell through the inverse of the particle velocity computed at each time step multiplied
194 by the cell length and weighted by the number of particles visiting the cell. This PDF is then used to
195 estimate the parameters of the TPL model

196 $$\psi(t_w) = \frac{n}{t_1} \frac{\exp(-t/t_2)}{\left(1+\frac{t}{t_1}\right)^{1+\beta}} \qquad (6)$$

197 where t_w is the waiting time of a particle within a given domain cell, $t_1, t_2,$ and β are model
198 calibration parameters, which are estimated through a standard least square technique. Note that
199 previous results have shown that the parameters obtained from (6) can be readily used to interpret
200 breakthrough curves associated with non-reactive solutes (Edery et al., 2014).

201 The velocity fields are examined upon computing the evolution of the velocity and conductivity
202 fields statistics, as described in the following. Let us consider a discrete field of a generic quantity z_{ij}
203 evaluated in a given cell ij. In the particle tracking numerical simulations we quantify $n_{ij}(t)$ as the
204 number of particles that have visited cell ij along the simulation up to a given time t. Thus, we
205 evaluate two relative frequency (or empirical probability) distributions, i.e., $f(z_{ij})$ and $f(nz_{ij})$,
206 hereafter termed as unweighted and weighted distribution of the variable z_{ij}, respectively. We define
207 the weighted variable $nz_{ij}(t) = n_{ij}(t)z_{ij}/\bar{n}(t)$, where $\bar{n}$ is the average value of n_{ij}. Note that the
208 adopted weighting scheme corresponds to weighting z_{ij} by the solute mass distribution. Average
209 values of the weighted and unweighted distributions (hereafter denoted as $\bar{z}$ and $\overline{nz}$, respectively) can

210   then be evaluated. In the following we perform particle weighting in the non-reactive as well as in
211   the reactive transport scenarios. Distribution weighting by reactive particles is indicated by n_R,
212   meaning that weighting is performed based on the reactive transport simulations (i.e., considering h
213   and co particles as explained above). The plain symbol n indicates weighting by non-reactive
214   particles, employed to simulate conservative tracer tests as detailed above. The variable z_{ij} is taken
215   to correspond to either the cell log-conductivity y_{ij} or fluid velocity v_{ij} in the results illustrated in
216   Section 3.

3.Results

218   We start our analyses by simulating transport of a non-reactive tracer across the generated
219   heterogeneous conductivity domains. As log-conductivity variance increases, the range of
220   conductivity values naturally increases, this being reflected in the distribution $f(y_{ij})$ (see, e.g., Figure
221   1 a-c (blue circles)). The shape of weighted conductivity distributions, $f(ny_{ij})$, differs from the one
222   of $f(y_{ij})$, consistent with the observation that particles are chiefly channelled towards preferential
223   flow pathways. The latter distributions tend to be shifted towards high conductivity values and are
224   characterized by an enhanced mean conductivity value as compared against their generated
225   (unweighted) counterparts (see conductivity mean and weighted mean values in Table 1, and the
226   results corresponding to the blue and red circles depicted in Figure 1 a-c). This shift is imprinted onto
227   the probability density function (PDF) of the waiting times and onto its associated CTRW-TPL
228   parameters (see Figure 2 a-c), consistent with prior studies (Edery et al., 2014; Edery, Geiger, et al.,
229   2016; Edery, 2020). We then simulate reactive transport across the collection of generated fields,
230   allowing for precipitation (and/or dissolution) of calcite and assessing the evolution of the
231   conductivity field according to the Kozeny-Carman formulation introduced in Section 2.
232   Conductivity, head, and velocity fields, as well as particle visitations, $n_{ij}(t)$, associated with species
233   h and co are sampled across time.

234   After 200 Δt have elapsed (corresponding to a total simulation time of 20 min, i.e., a full pore
235   volume) a set of h particles connecting the inlet to the outlet of the system is clearly visible (see
236   Figure 3 a and b), these particles being non-uniformly distributed in space. Figure 3a and b depict a
237   heat map of the h particles distribution at time $t = 20$ min, clearly evidencing the emergence of regions
238   of preferential flow (PF). We also note that the number of h particles density (corresponding to
239   concentration) tends to decrease with increasing distance from the inlet, these being replaced by co
240   particles, consistent with the observation that they are consumed during the course of the reactive
241   process which induces dissolution of the host solid matrix. The h and co particles attain equilibrium
242   within cells away from the inlet. As such, reaction can only take place if a particle leaves (or enters)
243   a cell under the action of advection and/or diffusion leading to a new equilibrium state. When
244   examining the alteration of conductivities due to the dissolution/precipitation reaction, we note that
245   dissolution (corresponding to an increase of permeability values) is primarily tied to the preferential
246   flow pathways. Otherwise, precipitation is seen to take place in regions close (on average) to these
247   pathways. The highest strength of precipitation is observed in the proximity of the preferential
248   pathways, to then decrease with distance from these.

249   Figures 3c and e depict the regions where conductivity has increased (due to dissolution) or
250   decreased (due to precipitation), respectively. The h particles invading the domain closely follow the
251   PFs displaying a fingering pattern, leading to a corresponding dissolution pattern associated with
252   locally increased conductivities. Since conductivity values along the PFs are typically higher (on
253   average), dissolution is increasing these conductivities even further, giving rise to a self-sustained

254 enhancing mechanism. The concentration of h particles reaches a local (i.e., within a given cell)
255 equilibrium with the produced co particles. Hence, dissolution will take place where transport induces
256 shifts in concentration that need to be compensated by the dissolution/precipitation process to
257 maintain local equilibrium. Such scenarios can be attained (*i*) by co particles exiting the preferential
258 flow pathways due to the action of diffusion (i.e., they leave locations where concentration of h
259 particles is large upon diffusing towards higher pH regions where they precipitate) or (*ii*) by h
260 particles traveling through the fast preferential paths and advancing through these. Figure 3g and h
261 display regions with dominating dissolution or precipitation for cells outside and within the PFs,
262 respectively. Here cells associated with PFs are identified upon relying on particle visitations
263 following Edery et al. (2014). Dissolution dominates within the PFs (as indicated by the red cells in
264 Figure 3h), because h particles are injected through a flux-weighted boundary condition. On the other
265 hand, the produced co particles do not precipitate at locations corresponding to the high h
266 concentration residing in the PFs. These may precipitate away from these regions, where they
267 experience low concentrations of h particles. Thus, we observe a reduction of conductivity taking
268 place in regions adjacent to the PFs (Figure 3b and g). In summary, our computational results
269 document an increase of conductivity along the preferential pathways jointly with a conductivity
270 reduction within regions close to these and along directions approximately normal to them.

271 Changes of conductivity values ensuing precipitation/dissolution are clearly visible by the
272 broadening of the unweighted log-conductivity distribution $f(y_{ij})$, see Figure 1d-f, and Figure 1g-i
273 (blue circles), evaluated at times $t = 10$ and $t = 20$ min, respectively. The reaction dynamics leads to
274 a conductivity field characterized by a slightly increased average value, given that our computational
275 analyses entail the injection of an acid fluid into the system (see Table 1 for details). Detailed
276 inspection of Figure 1d and f reveals that precipitation takes place across a slightly larger area than
277 dissolution, i.e. values of the frequency distribution $f(y_{ij})$ associated with low conductivities tend to
278 increase at a larger rate rather than those corresponding to high conductivities (the left tail of the
279 distributions becomes heavier than the right tail with the progress of reaction). The
280 weighted ($f(ny_{ij})$) and unweighted ($f(y_{ij})$) distributions (red and blue circles in Figure 1d-f, and
281 Figure 1g-i at time $t = 10$ and $t = 20$ min, respectively) are visibly broadening, being associated with
282 an average conductivity which is higher than the one of the originally generated conductivity domains
283 (see Table 1). As stated above, dissolution is focused along the preferential pathways, which comprise
284 an area of limited extent with respect to the whole field.

285 The above documented mechanism and its signature on the weighted and unweighted
286 conductivity frequency distributions are sensitive to the initial log-conductivity variance, σ_0^2. When
287 considering both distributions $f(y_{ij})$ and $f(ny_{ij})$, associated with the case $\sigma_0^2 = 1$, the distributions
288 variance are seen to increase in time, as compared to the values attained at the beginning of the
289 simulation (i.e., prior to reaction; see Figure 1a to d and g, and Table 1). Otherwise, as the initial
290 heterogeneity increases (see, e.g., $\sigma_0^2 = 3,5$) mean and variance associated with the weighted and
291 unweighted conductivity distributions display only minor changes (approximately 10%) across the
292 temporal window considered. The conductivity fields characterized by the lowest σ_0^2 value are
293 associated with preferential pathways that are not starkly recognizable when analyzed under non-
294 reactive transport conditions. These channels become more clearly distinguishable as reactions induce
295 an increase of the conductivities along the PFs. At the same time, precipitation causes a decrease of
296 the conductivity outside the PF. This leads to an increased importance of the left tail of $f(y_{ij})$,
297 corresponding to an increase of low conductivity values (see Figure 1, left middle and bottom rows).

298   With reference to the highest conductivity variance analyzed, the reaction patterns for the
299 precipitation and dissolution lead to a smaller relative change between conductivity frequency
300 distributions evaluated prior and after the reaction. Relative changes between the unweighted and
301 weighted conductivity frequency distributions (including the ensuing mean and variance listed in
302 Table 1) evaluated before and after the reaction are less pronounced as the variance of the generated
303 conductivity field increases (see Figure 1 middle and right columns and Table 1). This is related to
304 the observation that, as log-conductivity variance increases, preferential pathways in the originally
305 generated field become markedly more distinct. Thus, relative differences between unweighted and
306 weighted conductivity histograms are seen to diminish in time because the flow field is already
307 organized according to well-identified pathways and tends to preserve its initial pattern (Figure 1d-f,
308 and Figure 1g-i at time $t = 10$ and $t = 20$ min, respectively). Note that low order statistics (i.e., mean
309 and variance) of velocity and conductivity display only a minute evolution with the progress of
310 reaction, in spite of the relevant changes exhibited by the tails of the frequency distributions (see
311 Figure 1) for all considered values of σ_0^2, the latter feature being relevant when addressing non-
312 Fickian transport, as further discussed below.

313   As stated in Section 2.2, the conductivity fields altered through precipitation/dissolution and
314 extracted at regular time intervals of $10 \, \Delta t$ are subject to non-reactive transport analyses and the
315 ensuing evolution of the parameters of the TPL model (6) is analyzed. Key results of these analyses
316 are listed in Table 1 with reference to the original (unaltered) conductivity fields and at the final
317 simulation time (i.e., at time $t = 200 \, \Delta t$). Analysis of the results associated with transport across the
318 log-conductivity field characterized by the smallest original variance (i.e., $\sigma_0^2 = 1$) and listed in Table
319 1 indicates that the changes of the sample log-conductivity PDF induced by the progress of the
320 reaction are reflected by the parameters of the TPL model (6). These transition from estimated values
321 corresponding to an effective Fickian transport regime (corresponding to $\beta = 2$, see also Figure 2a)
322 to values denoting a highly non-Fickian effective transport setting, manifested by the widening of the
323 support of the waiting time PDF $\psi(t_w)$ (see also Figure 2d and 2g, for results obtained at $t = 10$ and
324 20 min, respectively). Effective transport in the domain with the highest variance (i.e., $\sigma_0^2 = 5$; see
325 Table 1) is characterized by estimated TPL parameters corresponding to a non-Fickian signature also
326 prior to the occurrence of precipitation/dissolution (Figure 2c). Such a signature is then further
327 enhanced after reaction has altered the conductivity field, yet displaying a less marked evolution of
328 the shape of the $\psi(t_w)$ as compared to the case $\sigma_0^2 = 1$ (see also Figure 2f and i for $t = 10$ and 20 min,
329 respectively).

330   The observed temporal changes in conductivity and the ensuing local dynamics of transport
331 pattern yield global variations in the reaction rate. Consistent with prior studies and the imposed
332 boundary conditions, the mean velocity associated with the originally generated conductivity domains
333 increases with σ_0^2. As the reaction progresses and the conductivity fields change, the increased area
334 subject to dissolution leads to a slight increase of the mean velocity for all of the σ_0^2 analyzed. To
335 analyze the influence of the preferential flow on the velocity that is affecting particle transport, we
336 consider the average value $\overline{n_R v}$, evaluated upon considering weighting by the number of reactive
337 particles, n_R, visiting each cell (where the term reactive particles denotes both h and co particles
338 employed in the context of the reactive transport simulations). The weighted average velocity displays
339 an initial increase over time due to the increase of conductivity within the preferential pathways.
340 When considering the relative change across the whole simulation time, values of the temporal
341 increase of $\overline{n_R v}$ are similar across the three heterogeneity levels examined, i.e., they are seemingly
342 independent of σ_0^2. However, results in Figure 4a also reveal that the average velocity $\overline{n_R v}$ displays
343 distinct temporal histories depending on σ_0^2. In particular, the value of $\overline{n_R v}$ tends to attain an

344 asymptotic value at time $t \approx 7$ min for $\sigma_0^2 = 5$, while showing a sustained increasing trend for $\sigma_0^2 =$
345 1. This result suggests that the feedback between reaction and flow patterns reaches an asymptotic
346 condition faster in systems characterized by higher heterogeneity.

347   The temporal evolution of the velocity fields due to the precipitation/dissolution reaction and
348 the resulting conductivity changes lead to time-dependent reaction pattern and reaction rates. The
349 Damköhler number is infinite on a local scale in our computational analyses, because the reaction is
350 instantaneous. When considering the entire system, transport processes induce a net overall reaction
351 rate that can be quantified as the sum of the total conductivity changes across time
352 $(Sum(|\Delta k_{ij}|) [\frac{cm}{sec}])$. The latter incorporates both positive and negative changes of hydraulic
353 conductivity and therefore quantifies the overall intensity of precipitation and dissolution processes
354 in the domain. The quantity $Sum(|\Delta k_{ij}|)$ is evaluated across all realizations for each of the σ_0^2 values
355 considered and is depicted in Figure 4b as a function of time. These results indicate that the overall
356 reaction rate increases in time with a similar rate for all considered values of σ_0^2 (figure 4b) at early
357 times. The observed increase is consistent with the initially advancing of the reaction front across the
358 domain. We observe that the reactive processes magnitude is proportional to σ_0^2. For low initial levels
359 of heterogeneity, conductivity values along the preferential pathways are closer to the average field
360 conductivity than what can be observed for the highly heterogeneous domains. As such, the portion
361 of the domain where precipitation or dissolution can take place increases at a rate proportional to σ_0^2.
362 As the reaction front reaches the domain outlet, the dissolving front found in the PF leaves the domain.
363 Hence, the global variation in conductivity (which is proportional to the magnitude of reactive
364 processes) tends towards an asymptotic value, corresponding to the diffusion-controlled solute
365 exchange along a direction transverse to the preferential pathways (see Figure 3). In agreement with
366 results shown in Figure 4a, this transition towards an asymptotic regime takes place earlier for larger
367 values of σ_0^2, while a smaller initial heterogeneity implies a longer transient period.

368   **4.Conclusions**

369 Our computational study tackles the quantitative characterization of the feedbacks between
370 precipitation and dissolution reaction dynamics taking place in randomly heterogenous conductivity
371 fields associated with various degrees of spatial heterogeneity. Our results are based on numerical
372 simulations and may be used to inform upscaling approaches to capture the pre-asymptotic and
373 asymptotic dynamics of reactive transport in heterogeneous systems through simplified models.

374   Our work leads to the following key conclusions.

375 • Joint occurrence of precipitation and dissolution is tightly coupled with the existence of
376   preferential flow pathways. Conductivity increase due to the dissolution reaction along such
377   paths leads to enhance particle migration along these. The dominance of preexisting
378   preferential flow regions on the (reactive) transport pattern across the field is therefore further
379   reenforced and self-sustained across time. At the same time, diffusion promotes displacement
380   of particles, leading to precipitation (and hence a progressive reduction over time of local
381   conductivities) at locations in the proximity of these.
382 • Reactive processes yield an increase over time of the range of conductivity values across the
383   domain, eventually leading to a widening of the support of solute waiting times and
384   conductivity distributions. The clear separation between regions where dissolution or
385   precipitation takes place is reflected in sample distributions of conductivity which tend to
386   become visibly left skewed with time, a feature which is associated with precipitation taking

place in low conductivity cells located in the proximity of existing preferential flow pathways.

- Solute mass weighted conductivity and velocity distributions are at the basis of our characterization of the parameters of a TPL model and enable us to capture effective (upscaled) non-Fickian transport behaviors. With the progress of precipitation/dissolution reactions, transport shifts towards an increasingly acute non-Fickian effective behavior (see Figure 2 and Table 1). The latter is then seen as a direct outcome of the documented feedbacks between transport and reactions taking place in heterogeneous porous media. The evolution of transport parameters towards a pronounced non-Fickian behavior is associated with only minor changes of the mean and variance of log-conductivity values. This result is consistent with the conceptual picture that the tails of flux and hydraulic conductivity distributions carry critical information to characterize transport while displaying only a minor effect on low order statistics associated with these quantities. Our results suggest that this feature must be acknowledged to properly characterize transport in the presence of precipitation/dissolution.

- We observe the emergence of an asymptotic regime in highly heterogeneous systems, where the (averaged) solute velocity attains a constant value even in the presence of reaction. This suggests the occurrence of an equilibrium state between reactive processes and transport under the flow conditions analyzed. This regime is attained because the effects of locally occurring precipitation and dissolution balance each other at the overall scale of the system, so that the ensuing (ensemble-averaged) solute velocity remains unaffected. The time required to attain such an asymptotic state increases with decreasing initial heterogeneity of the conductivity field, thus suggesting that pre-asymptotic behaviors may be more relevant in initially homogeneous systems.

Table 1. Values of mean and variance of unweighted and weighted log-conductivity distributions and estimated parameters of the effected TPL model obtained through calibration of (6) against the computed distributions of particle waiting times in the domain cells. Results are listed for the three values of the initial log-conductivity variance (σ_0^2) and are obtained from non-reactive transport simulations performed across conductivity fields resulting from reactive transport simulations at selected times.

	$\sigma_0^2 = 1$			$\sigma_0^2 = 3$			$\sigma_0^2 = 5$		
t [min]	0	10	20	0	10	20	0	10	20
$\bar{y}$	0.15	0.16	0.17	0.45	0.46	0.46	0.66	0.67	0.69
$\overline{ny}$	0.32	0.33	0.35	0.83	0.84	0.86	1.2	1.19	1.21
$\sigma^2(y_{ij})$	0.97	1.2	1.37	2.8	3.1	3.26	4.6	4.96	5.11
$\sigma^2(ny_{ij})$	0.99	1.21	1.41	2.8	3.07	3.21	4.6	4.85	5
β	2	1.4	1.05	1.7	1.2	0.95	1.4	0.8	0.6
t_1	0.1	0.09	0.06	0.1	0.07	0.03	0.08	0.03	0.01
$\mathrm{Log}_{10}(t_2)$	1	2.5	2.8	1.5	2.2	2.9	1.6	2.5	3
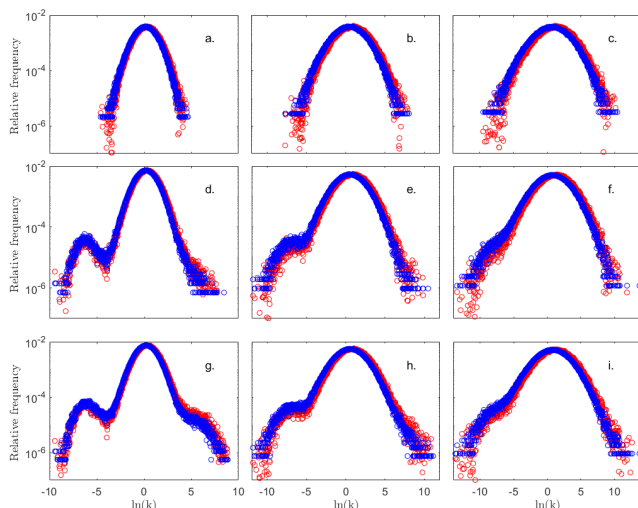
420   *Figure 1. Relative frequency distributions $f(y_{ij})$ (blue circles) and $f(ny_{ij})$ (red circles) for a tracer test performed on the*
421   *conductivty field prior to reaction and those associated with reactive simulation times of 10 and 20 minutes. Results correspond to*
422     $\sigma_0^2 = 1,3,5$ *(left, middle and right columns, respectively) and to t = (a-c) 0, (d-f) 10, and (g-i) 20 min. Mean and variance of these*
423   *distributions are listed in Table 1.*
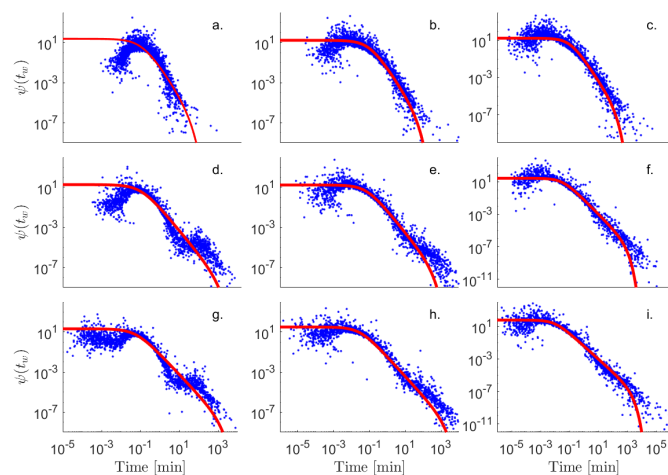
424
425   *Figure 2. Sample and modeled probability density function $\psi(t_w)$ of particle waiting times for a tracer test performed on the*
426   *conductivty field prior to reaction those associated with reactive simulation times of 10 and 20 minutes. Results correspond to $\sigma_0^2 =$*
427   *$1,3,5$ (left, middle and right columns, respectively) and t = (a-c) 0, (d-f) 10 min, and (g-i) 20 min. Values of TPL parameters*
428   *estimated by calibrating model (6) on the sample distributions are listed in Table 1.*

429
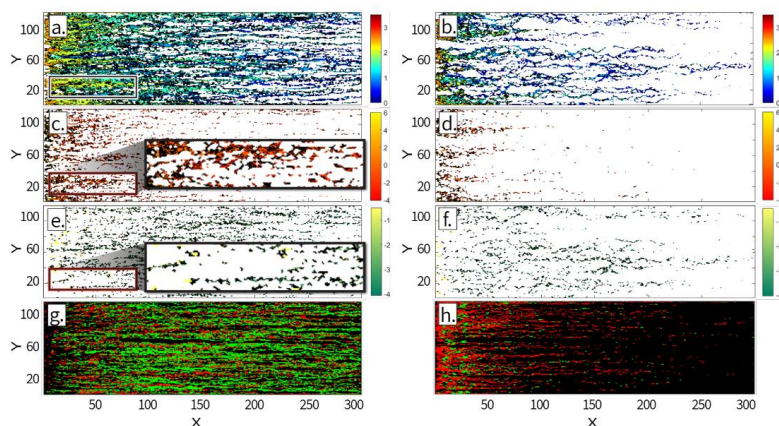
430
431 *Figure 3. Heat map representing (a,b) $Log_{10}(n_{Rij})$, i.e., the number of h particles visiting each cell for $\sigma_0^2 = 1$ and 5, respectively,*
432 *and (c-f) relative change in hydraulic conductivity at time t = 20 min with respect to the initially generated values for $\sigma_0^2 = 1$ (c and*
433 *e) and $\sigma_0^2 = 5$ (d andf). Panels c and d display positive changes in conductivity with respect to the initial field, while panels e and f*
434 *display negative changes in conductivity, both positive and negative changes being represented in log-scale. Results correspond to a*
435 *selected realizaton of the the log-conductivity fields. The highlighted box illustrates the separation between regions where*
436 *precipitation or dissolution take place. Panels g and h display cells associated with a net increase (green) and decrease (red) of*
437 *conductivity for cells outside (g) or within the PF (h), for $\sigma_0^2 = 1$.*

438
439

440
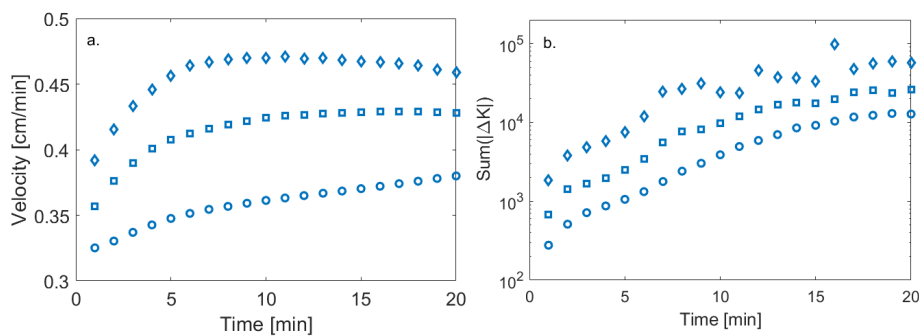
441

442 *Figure 4. Temporal evolution of (a) the weighted mean velocity $\overline{n_R v}$ (open symbols) and (b) the sum of all conductivity changes over*
443 *1 minut . Results correspond to $\sigma_0^2 = 1$ (circles), 3 (squares), and 5 (diamond). Please, check all symbols along the axes are defined*
444 *exactly with the same terminology in the text, ok?*

445

446   **References**

447   Ababou, R., McLaughlin, D., Gelhar, LynnW., & Tompson, AndrewF. B. (1989). Numerical
448   simulation of three-dimensional saturated flow in randomly heterogeneous porous media. *Transport*
449   *in Porous Media*, *4*(6). https://doi.org/10.1007/BF00223627

450   Atchley, A. L., Navarre-Sitchler, A. K., & Maxwell, R. M. (2014). The effects of physical and
451   geochemical heterogeneities on hydro-geochemical transport and effective reaction rates. *Journal of*
452   *Contaminant Hydrology*, *165*, 53–64. https://doi.org/10.1016/j.jconhyd.2014.07.008

453   Berkowitz, B., Cortis, A., Dentz, M., & Scher, H. (2006). Modeling non-Fickian transport in
454   geological formations as a continuous time random walk. *Reviews of Geophysics*, *44*(2), RG2003.
455   https://doi.org/10.1029/2005RG000178

456   Berkowitz, B., Dror, I., Hansen, S. K., & Scher, H. (2016). Measurements and models of reactive
457   transport in geological media: REACTIVE TRANSPORT MEASURES AND MODELS. *Reviews*
458   *of Geophysics*, *54*(4), 930–986. https://doi.org/10.1002/2016RG000524

459   Cabeza, Y., Hidalgo, J. J., & Carrera, J. (2020). Competition Is the Underlying Mechanism
460   Controlling Viscous Fingering and Wormhole Growth. *Geophysical Research Letters*, *47*(3).
461   https://doi.org/10.1029/2019GL084795

462   Ceriotti, G., Guadagnini, L., Porta, G., & Guadagnini, A. (2018). Local and Global Sensitivity
463   Analysis of *Cr (VI)* Geogenic Leakage Under Uncertain Environmental Conditions. *Water*
464   *Resources Research*, *54*(8), 5785–5802. https://doi.org/10.1029/2018WR022857

465   Dalla Libera, N., Pedretti, D., Tateo, F., Mason, L., Piccinini, L., & Fabbri, P. (2020). Conceptual
466   Model of Arsenic Mobility in the Shallow Alluvial Aquifers Near Venice (Italy) Elucidated
467   Through Machine Learning and Geochemical Modeling. *Water Resources Research*, *56*(9).
468   https://doi.org/10.1029/2019WR026234

469   Dentz, M., Gouze, P., & Carrera, J. (2011). Effective non-local reaction kinetics for transport in
470   physically and chemically heterogeneous media. *Journal of Contaminant Hydrology*, *120–121*,
471   222–236. https://doi.org/10.1016/j.jconhyd.2010.06.002

472   Edery, Y. (2020). The topological origin of anomalous transport: Persistence of {\beta} in the face
473   of varying correlation length. *ArXiv:1906.07061 [Physics]*. Retrieved from
474   http://arxiv.org/abs/1906.07061

475   Edery, Y., Scher, H., & Berkowitz, B. (2011). Dissolution and precipitation dynamics during
476   dedolomitization: REACTION DYNAMICS DURING DEDOLOMITIZATION. *Water Resources*
477   *Research*, *47*(8). https://doi.org/10.1029/2011WR010551

478   Edery, Y., Guadagnini, A., Scher, H., & Berkowitz, B. (2014). Origins of anomalous transport in
479   heterogeneous media: Structural and dynamic controls. *Water Resources Research*, *50*(2), 1490–
480   1505. https://doi.org/10.1002/2013WR015111

481   Edery, Y., Porta, G. M., Guadagnini, A., Scher, H., & Berkowitz, B. (2016). Characterization of
482   Bimolecular Reactive Transport in Heterogeneous Porous Media. *Transport in Porous Media*,
483   *115*(2), 291–310. https://doi.org/10.1007/s11242-016-0684-0

484   Edery, Y., Geiger, S., & Berkowitz, B. (2016). Structural controls on anomalous transport in
485   fractured porous rock: ANOMALOUS TRANSPORT IN FRACTURED POROUS ROCK. *Water*
486   *Resources Research*, *52*(7), 5634–5643. https://doi.org/10.1002/2016WR018942

487   Erol, S., Fowler, S. J., Harcouët-Menou, V., & Laenen, B. (2017). An Analytical Model of
488   Porosity–Permeability for Porous and Fractured Media. *Transport in Porous Media*, *120*(2), 327–
489   358. https://doi.org/10.1007/s11242-017-0923-z

490   Garing, C., Gouze, P., Kassab, M., Riva, M., & Guadagnini, A. (2015). Anti-correlated Porosity–
491   Permeability Changes During the Dissolution of Carbonate Rocks: Experimental Evidences and
492   Modeling. *Transport in Porous Media*, *107*(2), 595–621. https://doi.org/10.1007/s11242-015-0456-
493   2

494 Golfier, F., Zarcone, C., Bazin, B., Lenormand, R., Lasseux, D., & Quintard, M. (2002). On the
495 ability of a Darcy-scale model to capture wormhole formation during the dissolution of a porous
496 medium. *Journal of Fluid Mechanics*, *457*, 213–254. https://doi.org/10.1017/S0022112002007735

497 Gómez-Hernández, J. J., & Journel, A. G. (1993). Joint Sequential Simulation of MultiGaussian
498 Fields. In A. Soares (Ed.), *Geostatistics Tróia '92* (Vol. 5, pp. 85–94). Dordrecht: Springer
499 Netherlands. https://doi.org/10.1007/978-94-011-1739-5_8

500 Krauskopf, K. B., & Bird, D. K. (1967). *Introduction to geochemistry* (Internat.3Rev.ed).

501 Le Borgne, T., Dentz, M., & Carrera, J. (2008). Lagrangian Statistical Model for Transport in
502 Highly Heterogeneous Velocity Fields. *Physical Review Letters*, *101*(9), 090601.
503 https://doi.org/10.1103/PhysRevLett.101.090601

504 Liu, P., Yao, J., Couples, G. D., Ma, J., & Iliev, O. (2017). 3-D Modelling and Experimental
505 Comparison of Reactive Flow in Carbonates under Radial Flow Conditions. *Scientific Reports*, *7*(1),
506 17711. https://doi.org/10.1038/s41598-017-18095-2

507 Menke, H. P., Reynolds, C. A., Andrew, M. G., Pereira Nunes, J. P., Bijeljic, B., & Blunt, M. J.
508 (2018). 4D multi-scale imaging of reactive flow in carbonates: Assessing the impact of
509 heterogeneity on dissolution regimes using streamlines at multiple length scales. *Chemical Geology*,
510 *481*, 27–37. https://doi.org/10.1016/j.chemgeo.2018.01.016

511 Morse, J. W., & Mackenzie, F. T. (1993). Geochemical constraints on CaCO3 transport in
512 subsurface sedimentary environments. *Chemical Geology*, *105*(1–3), 181–196.
513 https://doi.org/10.1016/0009-2541(93)90125-3

514 Muljadi, B. P., Bijeljic, B., Blunt, M. J., Colbourne, A., Sederman, A. J., Mantle, M. D., &
515 Gladden, L. F. (2018). Modelling and upscaling of transport in carbonates during dissolution:
516 Validation and calibration with NMR experiments. *Journal of Contaminant Hydrology*, *212*, 85–95.
517 https://doi.org/10.1016/j.jconhyd.2017.08.008

518 Noiriel, C., & Daval, D. (2017). Pore-Scale Geochemical Reactivity Associated with CO_2 Storage:
519 New Frontiers at the Fluid–Solid Interface. *Accounts of Chemical Research*, *50*(4), 759–768.
520 https://doi.org/10.1021/acs.accounts.7b00019

521 Rege, S. D., & Fogler, H. S. (1989). Competition among flow, dissolution, and precipitation in
522 porous media. *AIChE Journal*, *35*(7), 1177–1185. https://doi.org/10.1002/aic.690350713

523 Riva, M., Guadagnini, A., Neuman, S. P., Janetti, E. B., & Malama, B. (2009). Inverse analysis of
524 stochastic moment equations for transient flow in randomly heterogeneous media. *Advances in
525 Water Resources*, *32*(10), 1495–1507. https://doi.org/10.1016/j.advwatres.2009.07.003

526 Saripalli, K. P., Meyer, P. D., Bacon, D. H., & Freedman, V. L. (2001). Changes in Hydrologic
527 Properties of Aquifer Media Due to Chemical Reactions: A Review. *Critical Reviews in
528 Environmental Science and Technology*, *31*(4), 311–349. https://doi.org/10.1080/20016491089244

529 Singurindy, O., & Berkowitz, B. (2004). Dedolomitization and flow in fractures. *Geophysical
530 Research Letters*, *31*(24), L24501. https://doi.org/10.1029/2004GL021594

531

532

533

534

535